One-Step Synthesis of Ag@TiO$_2$ Nanoparticles for Enhanced Photocatalytic Performance

Yufan Zhang [1], Fan Fu [1], Yuzhou Li [1], Desuo Zhang [1,2,*] and Yuyue Chen [1,*]

[1] National Engineering Laboratory for Modern Silk, College of Textile and Clothing Engineering, Soochow University, Suzhou 215123, China; yufanzhang21@163.com (Y.Z.); fanfu326@163.com (F.F.); 20165215052@stu.suda.edu.cn (Y.L.)

[2] Nantong Textile & Silk Industrial Technology Research Institute, Nantong 226314, China

* Correspondence: dszhang@suda.edu.cn (D.Z.); chenyy@suda.edu.cn (Y.C.); Tel.: +86-159-6220-9366 (D.Z.); +86-189-6252-9370 (Y.C.)

check for updates

Abstract: Polyamide network polymers (PNP) modified TiO$_2$ nanoparticles (NPs) were decorated with Ag NPs in hydrothermal gel method, forming one-step synthesized photocatalysts, Ag@TiO$_2$ NPs. The effect of PNP and the amount of Ag NPs added were investigated in this work. PNP acted as a nanocage to prevent TiO$_2$ aggregation and capture Ag accurately, which could effectively control product sizes and improve dispersibility in solvents. Simultaneously, TiO$_2$ NPs modified with Ag NPs exhibited remarkable photocatalytic effects. One-step synthesis simplified the experimental process and avoided the agglomeration of silver ions during the secondary reaction, achieving the purpose of uniform distribution at a specific location of TiO$_2$ NPs. The prepared Ag@TiO$_2$ NPs-0.5 could remove 79.49% of Methyl Orange (MO) after 3 h of ultraviolet light irradiation, which was 2.7 times higher than the reaction rate of pure TiO$_2$ NPs. It also exhibited good photoactivity under Visible light conditions. Moreover, the mineralization rate of MO over the Ag@TiO2 NPs-0.5 could be up to 72.32% under UV light and 47.08% under Visible light irradiation, which revealed that the prepared catalysts could effectively degrade most of the MO to CO$_2$ and H$_2$O. The samples also demonstrated the excellent stability and easy recyclability with over 90% of the original catalytic level for MO degradation. The photocatalysts studied also exerted broad application prospects such as photovoltaic hydrogen production, electronic sensors and biomedicine.

Keywords: Ag@TiO$_2$ NPs composite; one-step synthesis; photocatalytic; MO removal

1. Introduction

With the rapid advancement of industrialization, human survival faces serious challenges of environmental pollution and energy shortage, which has caused harm to human health [1,2]. Compared with other industries, the textile and dye industry produce 70% of all world annual wastewaters, hence eliminating the dyes in wastewater is especially vital for environmental protection [3,4]. However, till now, traditional methods implemented previously have not been able to remove these organic pollutants from the roots, while semiconductor photocatalytic technology is a viable option to solve this problem [5]. Photocatalytic activity and photostability are important indicators for evaluating photocatalytic quality, but few catalysts have both high photocatalytic activity and excellent light stability, such as oxide semiconductor TiO$_2$.

Nanosized TiO$_2$, first reported by Fujishima, has caused much attention thanks to its low price, non-toxicity, excellent chemical stability, and wide availability [6–8]. However, anatase TiO$_2$ can only absorb the wavelengths of sunlight (λ < 400 nm) owing to the wide bandgap (3.2 eV), which greatly limits the utilization of solar energy. Moreover, photogenerated electrons and holes are easily re-combined,

resulting in low photocatalytic activity [9–11]. Narrowing the band gap of TiO_2 to broaden the absorption spectrum response interval and reducing the recombination rate of photoinduced electron-hole pairs, have become research hotspots to improve photocatalytic performance [12,13].

In recent years, in order to improve the catalytic effect of TiO_2 nanoparticles (NPs), surface modification and ion doping were further studied [14–16]. The introduction of noble metal to a semiconductor catalyst is one of the effective methods resulting from the synergistic effect of Schottky barrier and surface plasmon resonance [17,18]. On the one hand, the Schottky barrier is formed to accelerate electron/hole separation. On the other hand, TiO_2 NPs can absorb more photons because of the plasmon resonance effect [19,20]. With its low cost, low toxicity and simple preparation, Ag has become a suitable candidate.

There have been many studies on the modification of TiO_2 NPs with Ag, while most of them are synthesized by two-step methods, where Ag NPs first are prepared and then combined with TiO_2 NPs. Oxidation of metal particles, agglomeration of the secondary reaction, and the length of the experiment greatly limit the quality of the product, resulting in insufficient photocatalytic ability of the obtained photocatalyst. In this paper, a one-step synthesis of $Ag@TiO_2$ nanoparticles using nanocage as a junction is designed to generate $Ag@TiO_2$ in situ. PNP is a polyamide network polymer containing a large amount of amine groups, which is used to surface-modify, as a nanocage, to prevent TiO_2 NPs aggregation and capture Ag at a fixed position of TiO_2 NPs [21,22].

To the end, the optimal addition amount of PNP and Ag NPs was obtained by analyzing the origin of the enhancement mechanism and testing the different parameters. The as-prepared composite sample displayed an excellent performance in the catalytic degradation test, because the synergies of Ag and TiO_2 nanoparticles accelerated the transmission of photogenerated electrons, ultimately increasing the photocatalytic rate, and the results are discussed next.

2. Materials and Methods

2.1. Materials

Tetrabutyl titanate (TBT), glacial acetic acid (CH_3COOH, >99%), silver nitrate ($AgNO_3$), absolute ethanol (CH_3CH_2OH, >99%) were provided by Sigma-Aldrich, St. Louis, MO, USA. Methyl Orange (MO) was supplied by Adamas Reagent Co. Ltd., Shanghai, China. The reagents in this research were analytical grade and required no further purification. Polyamide network polymers (PNP) was formulated to 100 g/L for the following experiment, which were prepared in our previous paper [21].

2.2. Preparation of Photocatalysts

2.2.1. Preparation of Pure TiO_2 Nanoparticles

A total of 10 g TBT was dissolved in 30 mL absolute ethanol, and constantly mixed with ultrasonic for 0.5 h. The obtained mixed solution is referred to as liquid A. Moreover, 60 mL of Liquid B was placed in a three-necked flask containing deionized water, glacial acetic acid, and absolute ethanol at a volume ratio of 1:1:4. Then, liquid A was dripped into Liquid B at a rate of 1 mL per minute under stirring for up to 2 h, at ambient temperature. The gel was formed after 24–36 h, with the color changing from transparent to light blue.

A total of 1 mol PNP solution (100 g/L) was added into 10 g gel and kept under magnetic stirring until completely dissolved. Afterwards, the mixture was poured into a 100 mL polytetrafluoroethylene lining, which was kept at 200 °C for 8 h in an autoclave. After naturally cooling to room temperature, the obtained product was centrifuged multiple times to eliminate excess precursor and PNP until the pH of the solution returned to neutral. Finally, the TiO_2 NPs white in color were obtained under 60 °C dry conditions.

2.2.2. Preparation of Ag@ TiO$_2$ Nanoparticles

In this study, Ag@TiO$_2$ NPs were one-step produced with AgNO$_3$ as metal source and TBT as the precursor. According to this procedure, 10 g TBT was dispersed in absolute ethanol at a volume ratio of 1:3. The above solution was then added dropwise into a 60 mL mixture solution, which was made up of 10 mL deionized water, 40 mL absolute ethanol and 10 mL glacial acetic acid. After stirring for 3 h at 20 °C, the solution turned into gels. A suspension composed of 10 g gels, 1 mol PNP solution (100 g/L) and 0.1 M AgNO$_3$ solution was stirred for 2 h. Next, the mixture was poured into a 100 mL polytetrafluoroethylene lining and hydrothermally treated for 8 h at 200 °C. In order to optimize the molar ratio of Ag to TiO$_2$, Ag@TiO$_2$ with different molar ratios of AgNO$_3$ (0.25%, 0.5% and 1%) were prepared and the resulting samples were labelled as Ag@TiO$_2$ NPs-x, where x was 0.25, 0.5, and 1, respectively. In all cases, the samples were washed thoroughly to get rid of excess precursor and PNP solution and then stored at 60 °C in a vacuum oven until required.

2.3. Materials Characterization

The Hitachi S-4800 scanning electron microscopy (Hitachi Ltd. Tokyo, Japan) was used to show the images of the samples surface morphology and particle size distribution. In order to better analyze the morphology and particle size, transmission electron microscopy with EDS capabilities (TEM), high-resolution electron microscopy (HRTEM) and selected area electron diffraction (SAED) were tested on a Tecnai G2 F20 S-TWIN (FEI, Hillsboro, OR, USA) operating at 200 kV. The X-ray diffraction scanning rate of 5° min^{-1} characterized the crystal form of the products, with Cu-Kα (λ = 0.1542 nm), equal voltage of 40 KV and equal current of 200 mA. All data from 20° to 80° in the XRD spectrum were integrated and recorded, and the characteristic peaks were determined by comparison with the Joint Committee on Powder Diffraction Standards (JCPDS 21-1272 and JCPDSCard No. 04-0783) [23,24]. PHI-5700 ESCA apparatus was operated to test the X-ray photoelectron spectroscopy. It could be seen from the spectrum that all the values of binding energy were adjusted with the help of the hydrocarbon band (C 1 s: 284.8 eV), the X-ray source expressed Al Ka (hv = 1486.6 eV). Fourier transform infrared spectra (FTIR) of pure TiO$_2$ NPs and Ag@TiO$_2$ hybrid NPs were measured on a Nicolet 5700 instrument (Thermo Electron Corporation, Beverly, MA, USA). Evolution 220 UV-Vis spectrophotometer (Thermo Fisher Scientific, Boston, MA, USA) was used to detect the absorption capacity of the prepared hybrid catalysts. It should be noted that integrating sphere method using BaSO$_4$ powder as the background was carried out in this experiment, where the measurement range was 200–800 nm. Simultaneously, the total MO contents in the tests were also recorded (λ = 463 nm).

2.4. Photoelectrochemical Measurements

The photoelectrical response and electrochemical impedancespectroscopy (EIS) play vital roles in evaluating the separation efficiency of the photogenerated carriers. The photoelectrochemical measurements were performed in a standard three electrodes system with a 0.1 M Na$_2$SO$_4$ aqueous electrolyte solution using a PGSTAT302N electrochemical workstation (Swiss Wantong China Ltd., Shanghai, China). Platinum wire and saturated calomel electrode would serve as the counter electrode and the reference electrode, respectively. The working electrode was obtained by dipcoating 3 μm of the suspension onto glassy carbon electrode. Photo-responses were measured at 0.0 V and the EIS measurements were defined at a 5 mV AC voltage amplitude with a frequency range of 10^5 to 10^{-1} Hz. The working electrodes were irradiated by a 300 W Xe lamp. The set light-liquid interface distance was 15 cm, the light intensity was 50 mW cm^{-2} and the d of the glassy carbon electrode was 3 mm.

2.5. Photocatalytic Activity Measurements

The ability of photodegradation of dye determined the photocatalytic performance of the catalyst, and the as-prepared catalyst was placed into MO for photodegradation reaction to evaluate the effect. A 20 W UV light lamp (365 nm) and 300 W Xe lamp (equipped with a 420 nm filter) were applied as the light source to induce photocatalysis, and light intensity for both was 50 mW cm^{-2}. The set light-liquid interface distance was 15 cm. According to previous standards, 100 mg catalysts were dispersed in beaker containing 100 mL MO (20 mg/L) and the solution was thoroughly mixed for approximately 15 min. Considering the adsorption-desorption between the sample and the dye, the test solution needed to be pretreated in the dark prior to the experiment [25]. Afterwards, the suspension was stirred for 3 h under irradiation and 3 mL of the droplet was uniformly sampled at a given time interval into a tube, centrifuging for testing.

By measuring the maximum absorption of the MO characteristic peak at 463 nm, the absorption standard curve equations for MO could be depicted on a UV-Vis spectrophotometer. The mineralization rates of MO were obtained using the total organic carbon (TOC) equipment (Multi N/C 2100, TOC/TN, Analytikjena, Jena, Germany). Reusability was another key indicator for determining the performance of the catalyst, hence 100 mg of Ag@TiO$_2$ NPs was subjected to cyclic photocatalytic testing five times in a row. During the test, the MO concentration was always set to 20 mg/L. After each cycle, the catalyst was collected by centrifugation and dried at 60 °C for the next usage.

3. Results and Discussion

3.1. Preparation of Ag@TiO$_2$ NPs

For nanocatalysts, particle size and dispersibility in solvents are two important parameters. Surfactants or polymers are typically added during the preparation to control the size of the nanoparticles and increase the dispersibility in the solvent. In this work, polymer PNP was used as a template to find the appropriate amount added without metal loading. In order to clearly verify the change in diameter and dispersion of TiO$_2$ nanoparticles, SEM was employed for further examination. Figure 1 depicts the SEM images of the TiO$_2$ NPs synthesized by the PNP in the conditions of different molars. As shown in Figure 1a, the pure TiO$_2$ NPs have a small particle size but have serious agglomeration owing to the high surface energy, which results in poor dispersibility as well as extremely large size ranges. After that, by adjusting the amount of PNP added to 0.25, 0.5 and 1 mol (Figure 1b–d), respectively, more and more PNP is added for the preparation of the TiO$_2$ NPs, hence the growing nanoparticles are confined by the polymeric nanocages in order to prevent from aggregating [26,27]. Compared with the pure TiO$_2$ NPs, the agglomeration phenomenon and the dispersibility are gradually improved. It follows that the overall size is controlled in the range of 30–40 nm after adding 1 mol of PNP, and most of the synthesized nanoparticles show good dimensional uniformity, which indicates a suitable amount of PNP solution can effectively improve the dispersion ability and keep the particle size at a small level. However, as the amount of PNP added exceeds 1 mol (Figure 1e,f), the mean diameter would become larger, which is caused by the steric hindrance generated with a large number of cavities between the branches. Thus, 1 mol PNP (100 g/L) was selected to prepare Ag@TiO$_2$ NPs for the following work.

The key steps of designing the pure TiO$_2$ NPs and Ag@TiO$_2$ NPs by the hydrothermal gel method are illustrated in Scheme 1. The first step of our approach was to prepare the TiO$_2$ precursor obtained by hydrolyzing TBT, as Ti source, into a gel form. To prevent the aggregation in the next hydrothermal reaction, prepared PNP was introduced for protecting TiO$_2$. Finally, Ag@TiO$_2$ NPs was synthesized under high temperature and high pressure conditions, and the color turned a deep reddish brown.
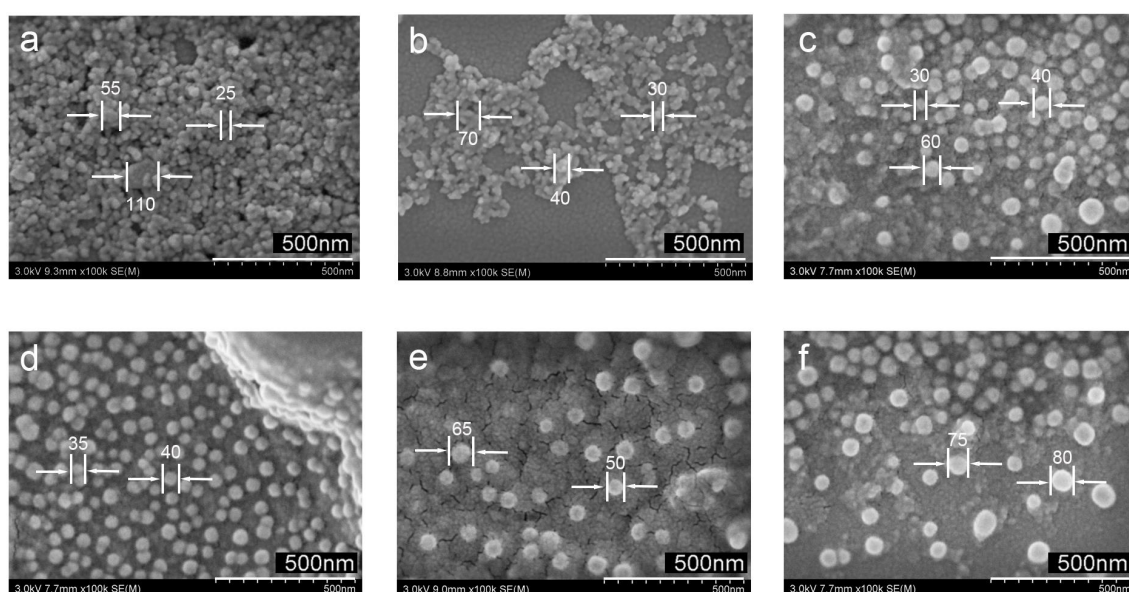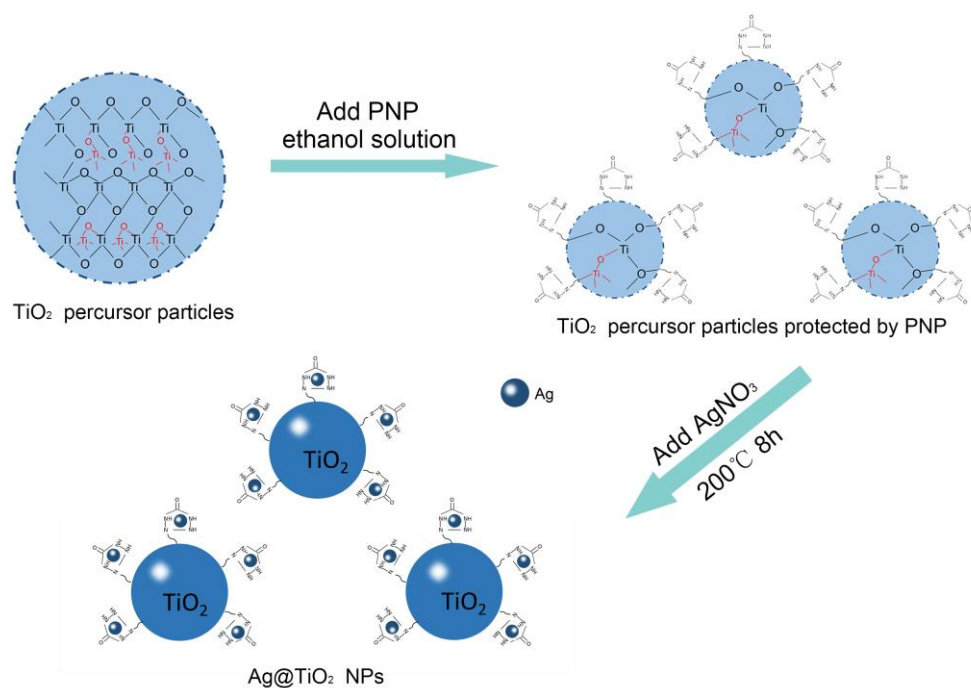
Figure 1. SEM images of TiO$_2$ nanoparticles (NPs) with different molars of polyamide network polymers (PNP): 0 mol (**a**), 0.25 mol (**b**), 0.5 mol (**c**), 1 mol (**d**), 2 mol (**e**) and 3.125 mol (**f**), respectively.

Scheme 1. Procedure for the synthesis of Ag@TiO$_2$ NPs.

Our previous works have found that by using PNP as a nanocage, a polyamide network polymer that contains numerous amine groups, metal particles can be complexed with amine groups and reduced to Ag NPs at a fixed position in the network structure during the initial stage of hydrothermal reaction [28]. Since the space of the network structure is limited, the size of the Ag NPs grown inside will be restricted, so that products with small size and uniform distribution are obtained. Meanwhile, the surface of the Ag NPs is rich in amino groups, which can be linked to the hydroxyl groups on the surface of the TiO$_2$ by hydrogen bonding, thereby achieving the effect of physically preventing aggregation [22]. These two findings inspired us to design a method to complete the growth of Ag and TiO$_2$ NPs in one-step.

After loading the silver particles, the morphology, structure and property of the photocatalyst were also changed. To further explore the morphologies, the lattice parameters and the element content of the samples, TEM, SAED, HRTEM and EDS were employed. The results are displayed in Figure 2 below. It is depicted that pure TiO_2 NPs (Figure 2a) have undergone severe agglomeration, whereas Ag@TiO_2 NPs-0.5 (Figure 2b) show excellent dispersibility and small particle size under the synergy of PNP and Ag NPs. It can clearly see that Ag NPs (d <10 nm) are embedded on the surface of TiO_2 NPs from the low magnification TEM image, as shown in Figure 2b, which also proves the existence of Ag NPs. A SAED pattern of Ag@TiO_2 NPs-0.5 is indicated in Figure 2c. The (111) crystal plane of Ag NPs and the (101) crystal plane of anatase are confirmed to match the d values obtained in the results. Meanwhile, the HRTEM image of TiO_2 and Ag (d is around 8 nm), accompanied by a fast Fourier transform (FFT) mode of local regions (inset), which exhibits the lattice fringes of TiO_2 (101) and Ag (111) planes with interplanar spacing of about 0.35 and 0.237 nm, respectively, are observed in Figure 2d,e [29]. The results are consistent with the results obtained from the diffraction pattern, indicating the as-prepared Ag@TiO_2 NPs is high quality. Figure 2f depicts the EDS of Ag@TiO_2 NPs-0.5, and the content of each element is also listed in the table where the Ag atom content is small, accounting for 0.6% of the Ti atom, which is also consistent with the experimentally set ratio.
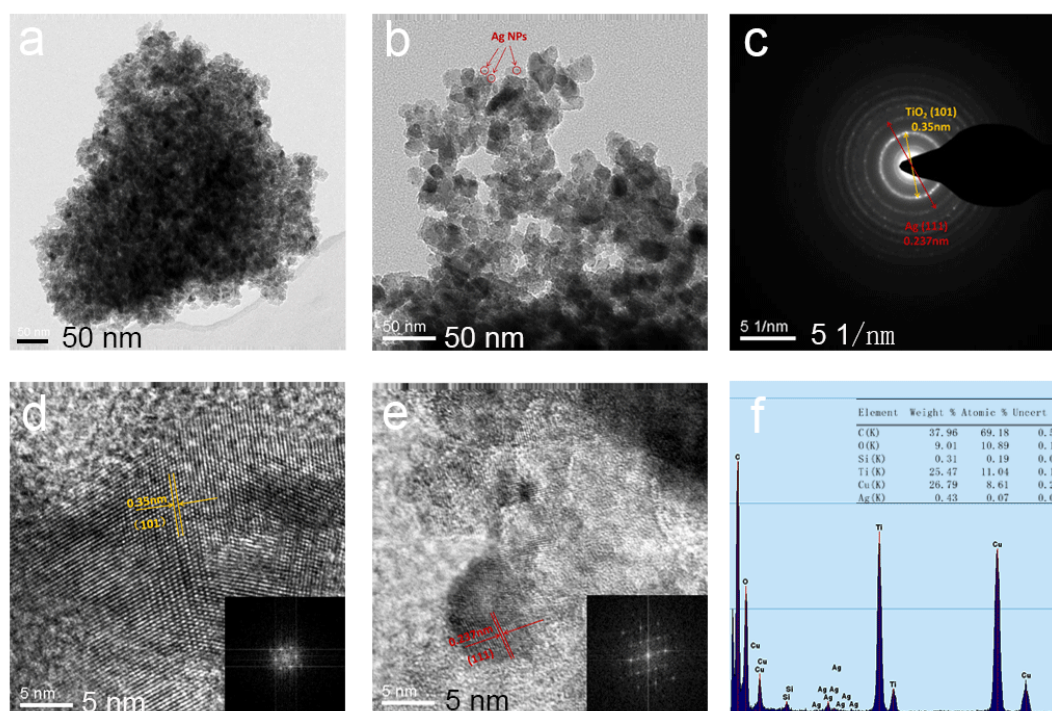

Figure 2. Transmission electron microscopy with EDS capabilities (TEM) image of the pure TiO_2 NPs (**a**) and Ag@TiO_2 NPs-0.5 (**b**); selected area electron diffraction (SAED) image of Ag@TiO_2 NPs-0.5 (**c**); high-resolution electron microscopy (HRTEM) image taken from TiO_2 NPs (**d**) and the corresponding fast Fourier transform (FFT) mode; HRTEM image taken from Ag NPs (**e**) and the corresponding FFT mode; EDS of Ag@TiO_2 NPs-0.5 (**f**).

XRD patterns were utilized to characterize the structure of as-prepared catalyst. Figure 3 shows the test results of TiO_2 NPs and Ag@TiO_2 NPs prepared through the one step in situ hydrothermal method. The Ag@TiO_2 NPs are mainly composed of anatase and nano silver, which are marked "Anatase" and "Ag" in the image. It is shown that the diffraction peaks at Bragg angles (2θ) of 25.3, 37.9, 48.05, 53.9, 55.06, 62.4, 68.76, 70.3, 75.06, 78.67 correspond to the (101), (004), (200), (105), (211), (204), (116), (220), (215), (206) lattice planes of anatase TiO_2 (JCPDS 21-1272). As observed, the crystal shape of the diffraction peaks appear clear and sharp, and there are no other impurity peaks, indicating well-formed crystal structures of the as-prepared TiO_2. In addition, the (200), (220)

lattice planes at Bragg angles (2θ) of 44.2 and 64.4 (JCPDSCard No. 04-0783) belong to Ag consistent with the TEM results, the peak intensities of which become stronger with an increase in the molar mass. It is noteworthy that since the diffraction band of the Ti (004) lattice plane is too high at 37.9°, the (111) characteristic peak of Ag is covered. Using the formula Scherrer Equation (1), the particle size corresponding to each crystal plane can be theoretically calculated [30,31]. Taking Ag@TiO$_2$ NPs-0.5 as an example, the mean diameter of TiO$_2$ NPs is estimated at 17, nm consistent with TEM results.

$$D = \frac{K\lambda}{\beta \cos\theta},$$
(1)

where K expresses a constant with a value of 0.89, the X-ray incident wavelength is represented by λ with a value of 0.154 nm, θ represents the half-diffraction angle and β is the full width at half maximum (rad).
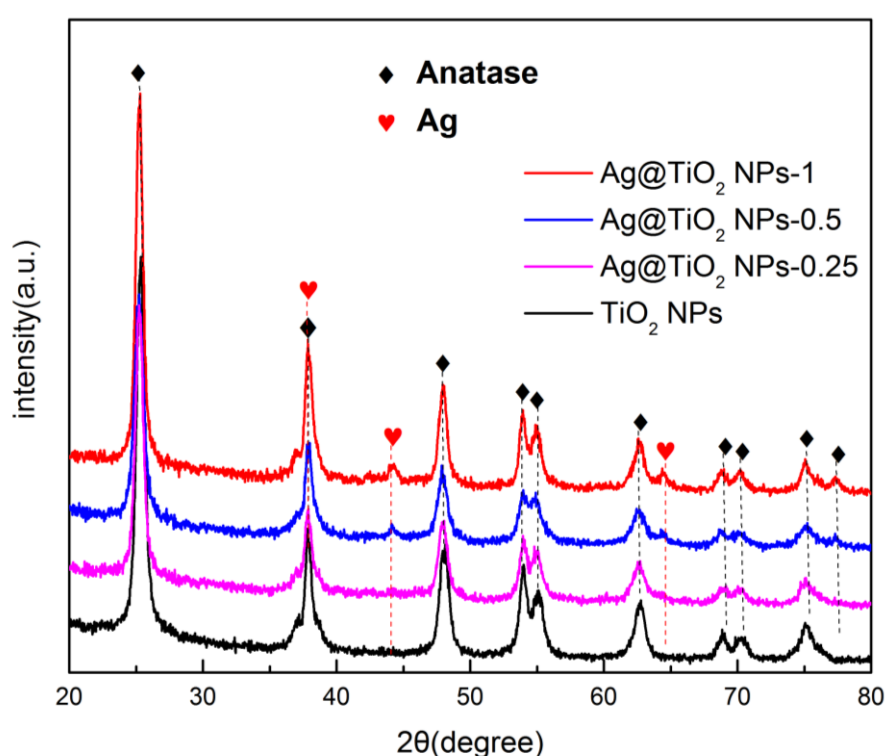

Figure 3. X-ray diffraction (XRD) patterns of pure TiO$_2$ NPs, Ag@TiO$_2$ NPs with different molar ratios of 0.25%, 0.5% and 1%.

XPS was implemented to further investigate the valence state of Ti and Ag atoms in Ag@TiO$_2$ NPs. The C, O, N, Ti and Ag elements can be observed in the survey spectrum (Figure 4a), whereas the C1s at 286.8 eV is used as a standard to determine the characterization data. Taking Ag@TiO$_2$ NPs-0.5 as an example, the XPS narrow-spectrum Ti 2p is shown in Figure 4b, and the binding energy generated by the spin-orbital splitting of the Ti 2p$_{1/2}$ and Ti 2p$_{3/2}$ peaks are 464.9 and 459.2 eV, which clearly proves that Ti exists in the form of Ti^{4+} in the sample [32–34]. Furthermore, compared with pure TiO$_2$ NPs, the binding energy at Ti 2p (Figure 4d) increases by approximately 0.8 eV as the amount of AgNO$_3$ is added. This phenomenon is caused by the difference in Fermi level between TiO$_2$ and Ag, where electrons are transferred from TiO$_2$ with high energy level to Ag until the energy levels are equal, resulting in a decline in the density of external electron clouds for Ti ions, and an increase in binding energy [35]. Figure 4c exhibits two characteristic peaks of the Ag 3d spectrum, where the binding energy of Ag 3d$_{3/2}$ is 374.2 eV and Ag 3d$_{5/2}$ is 368.2 eV. Carefully compared with Ag@TiO$_2$

NPs-1 and Ag@TiO$_2$ NPs-0.25 (Figure S1a,b), it can be seen that the splitting width between Ag 3d$_{3/2}$ and Ag 3d$_{5/2}$ are also 6 eV, indicating the presence of Ag^0 chemical states in the Ag@TiO$_2$ NPs [36].
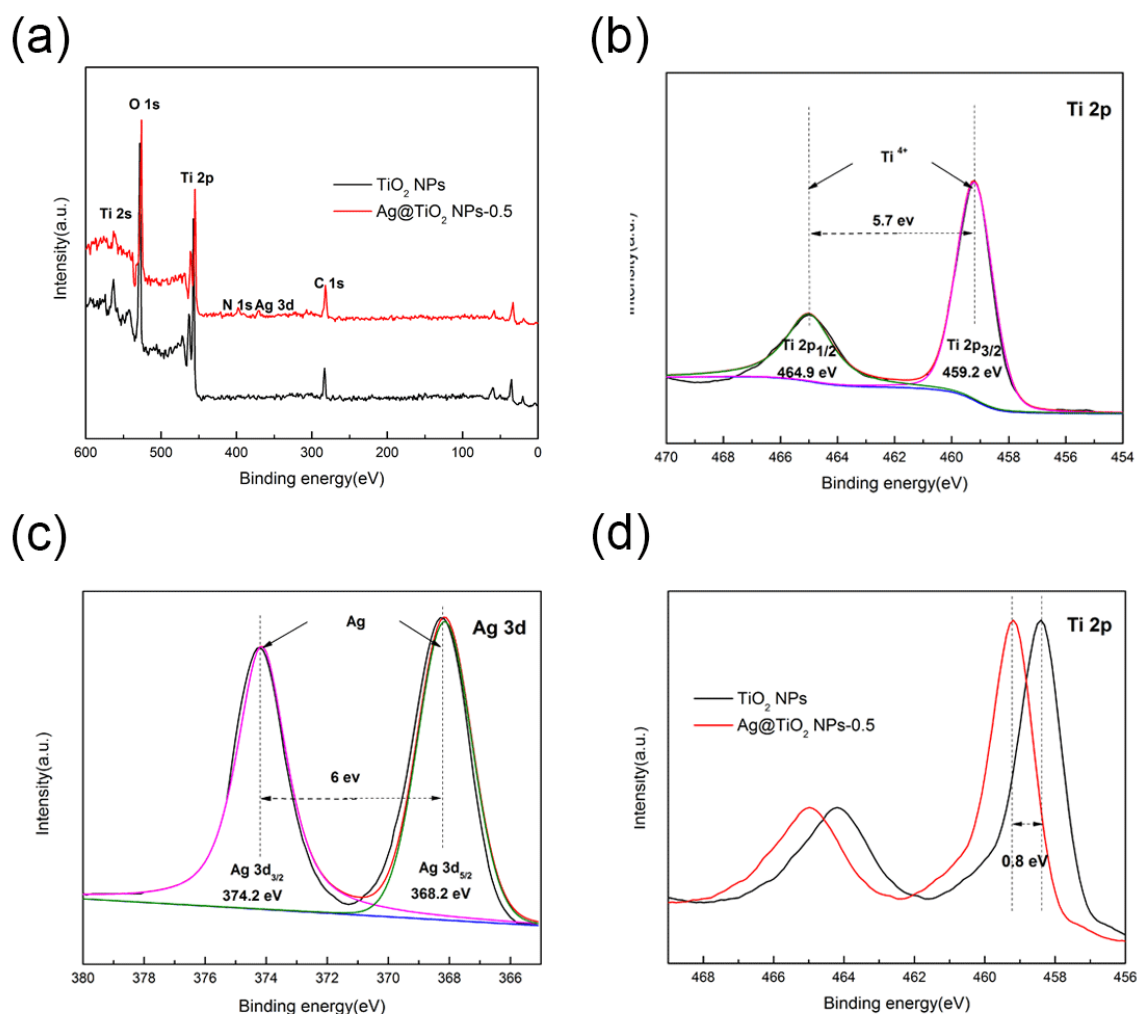

Figure 4. XPS spectrum of TiO$_2$ NPs and Ag@TiO$_2$ NPs-0.5 (**a**); high resolution spectra of Ti 2p (**b**); Ag 3d (**c**); Ti 2p of TiO$_2$ NPs and Ag@TiO$_2$ NPs-0.5 (**d**).

Figure 5 shows the FTIR spectrum of TiO$_2$ NPs and Ag@TiO$_2$ NPs catalysts. It shows that the strong absorption peak of TiO$_2$ NPs and Ag@TiO$_2$ NPs at 3396, 3410, 3419 and 3420 cm^{-1} have similar behavior, which is likely due to hydrogen bonded surface hydroxyl groups and OH of adsorbed water molecules [37–40]. In addition, the bending vibration peak of the O–H bond can be clearly observed around 1630 cm^{-1}. The signal at 1411 cm^{-1}, a narrow peak of the alcohol O–H bond bending vibration also appears, which is due to the addition of PNP ethanol solution [41].

3.2. Photocatalytic Activity of Ag@TiO$_2$ NPs

Photocatalytic ability is a vital factor in evaluating photocatalysts. Figure S2 shows the UV–Vis diffuse reflectance spectroscopy. The initial absorption edge of pure TiO$_2$ NPs is estimated to be 380 nm with a strong light absorption in the ultraviolet area. The modifications of the Ag NPs can enhance the photocatalytic activity under ultraviolet light, as well as Visible light. With regard to the Ag@TiO$_2$ samples with different loading amounts, compared to that of pure TiO$_2$ NPs, it can be observed that the absorption edges show a slight red shift which also enhances its Visible light photocatalytic activity to some extent [42–45]. Particularly, Ag@TiO$_2$ NPs-0.5 has the strongest light absorption among these catalysts. This is mainly owing to the suitable content deposition of Ag NPs,

which can effectively respond to Visible light caused by plasmon resonance effect and suppress the recombination of electron/hole pairs in order to promote the transfer and transport of photogenerated carriers. However, the excessive number of Ag nanoparticles leads to aggregating together, inhibiting the absorption of light, and providing an active site for the recombination of electron/hole pairs, thus, the light absorption ability is lowered.
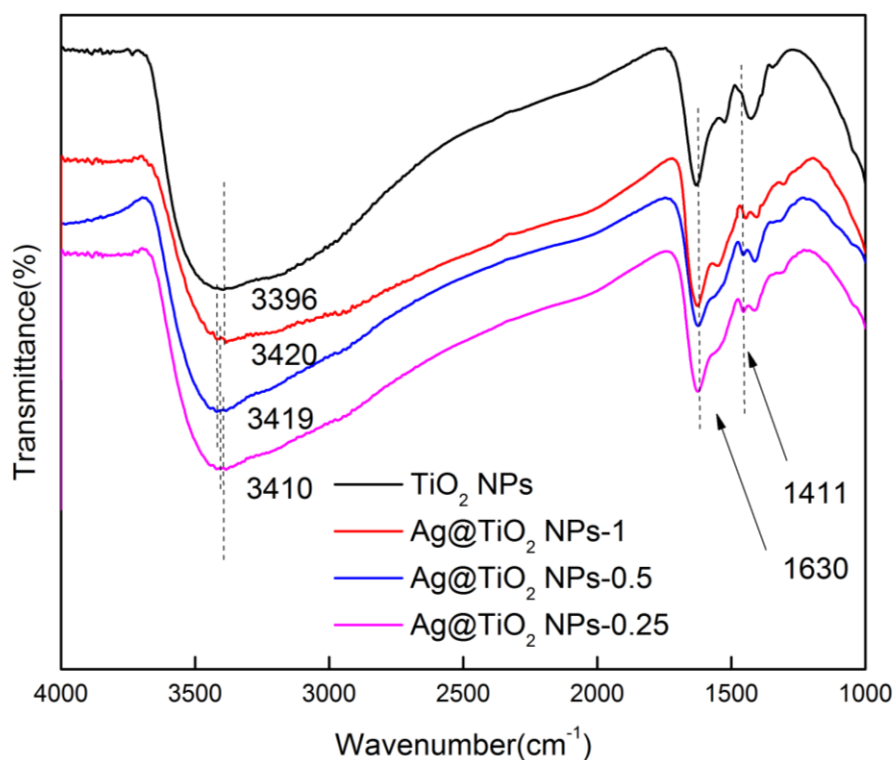

Figure 5. Fourier transform infrared spectra (FTIR) spectra of pure TiO_2 NPs and Ag@TiO_2 NPs.

Photocurrent measurement was carried out to evaluate the electron–hole recombination in the as-prepared samples (Figure 6a), where the photocurrent intensity remained steady and reproducible over several intermittent on-off cycle experiments. Apparently, the Ag@TiO_2 NPs-0.5 have the strongest photocurrent response which is ~4 times higher than that of pure TiO_2 NPs, suggesting that the Ag@TiO_2 NPs-0.5 have more effective charges separation and thus inhibit the recombination of electrons and holes under Visible light irradiation [46,47]. Moreover, electrochemical impedance spectra (EIS) measurements were performed to elucidate the charges transfer process of the photogenerated charge carriers. It is generally known that the radius of the Nyquist circle is directly related to charge transfer resistance, with a smaller semicircle radius corresponding to easier electron transfer. From Figure 6b, the radius of the arc in the EIS spectrum of Ag@TiO_2 NPs-0.5 is smaller than that of TiO_2 NPs and Ag@TiO_2 NPs, indicating that highly efficient interfacial charges transfers occur in Ag@TiO_2 NPs-0.5.

The photocatalytic abilities of Ag@TiO_2 NPs samples were assessed through the degradation of MO. To rule out the interference of MO self-degradation, we performed a self-degradation test on MO. In the condition of no photocatalyst and irradiation for 180 min, nearly no degradation of MO was found, which indicates that MO dye is suitable as a targeted pollutant and available to assess the catalytic ability of the catalyst owing to its steady structure. Figure 6c shows the photodegradation efficiencies after the UV light irradiating for 3 h. The photodegradation efficiency decreases in the order below:

Ag@TiO_2 NPs-0.5 > Ag@TiO_2 NPs-1 > Ag@TiO_2 NPs-0.25 > TiO_2 NPs.

The MO photodegradation efficiencies are estimated to be 79.49%, 62.98%, 52.05% and 42.14%, respectively. Clearly, as the molar ratio of Ag increases in a certain range, the degradation of the sample also increases, which implies that Ag plays an important role in photocatalytic degradation. Studies have shown that the photodegradation process of MO conforms to the model of Langmuir–Hinshelwood first-order reaction kinetics. Therefore, the reaction rate constant could be obtained by calculation through the following equation:

$$\ln(C_0/C) = k \times t, \tag{2}$$

in which k and t express the rate constant (min^{-1}) of photocatalytic degradation of MO and the irradiation time (min), respectively, while C_0 as well as C represent the concentration of MO after adsorption equilibrium and reaction time, respectively. Figure 6d proposes the linear fit of the photocatalytic degradation time against $\ln(C_0/C)$. It is worth noting that the catalytic reaction rate of Ag@TiO$_2$ NPs-0.5 is 2.7 times higher than TiO$_2$ NPs, which exhibits the optimum catalytic performance among photocatalysts above [48].

The photodegradation efficiencies under Visible light irradiation for 3 h are shown in Figure 6e, which has similar behavior to the catalysis under UV conditions. Ag@TiO$_2$ NPs-0.5 shows the strongest photocatalytic effect, and 50% of MO is decomposed after 180 min irradiation. To better compare the photocatalytic performance of these samples, the reaction kinetics of MO degradation is also investigated in Figure 6f. Obviously, Ag@TiO$_2$ NPs-0.5 has the maximum k value of 0.00395 min^{-1}, which is almost 2.6 times as high as that of TiO$_2$ NPs.

In addition, the UV-absorption spectrum of the Ag@TiO$_2$ NPs-0.5 suspension was recorded during the process of photocatalytic degradation. As the UV light irradiation time increases, it is apparent that the MO absorption band intensity decreases gradually. As shown in Figure S3a, after 60 min, the band intensity decreases rapidly with time and has been levelled off after 150 min. According to previous experiments, the chromophoric group of MO is the azo group (–N=N–), which corresponds to the wavelength of 463 nm [49]. The absorption maximum of band intensity at 463 nm was measured to estimate the concentration of MO in the solution and the catalytic effect can be visually observed. The corresponding color changes using Ag@TiO$_2$ NPs-0.5 are also depicted in the Figure S3b. Moreover, a total organic carbon (TOC) analysis was performed under UV and Visible light condition to further confirm the degree of oxidation (Figure S4). Through the measurement of TOC analyzer, the mineralization rate of MO over the Ag@TiO$_2$ NPs-0.5 can be up to 72.32% under UV light and 47.08% under Visible light irradiation. Compared with the photocatalytic degradation curves of TiO$_2$ NPs and Ag@TiO$_2$ NPs samples (Figure 6c,e), the TOC degradation efficiency of MO is relatively lower than the degradation rates, which proves that MO is decomposed into CO$_2$ and H$_2$O, accompanied with the formation of a certain intermediates in the process of photocatalytic degradation [50,51].

The stability and repeatability of the catalyst are of decisive significance in practical applications. In order to get insights into the reusability, the recycling capability of the photocatalyst is carried out with the Ag@TiO$_2$ NPs samples. In our test, the nanocomposite photocatalysts of MO were collected by centrifugation and then replaced into the same concentration of MO solution after each photodegradation. As displayed in Figure 6g,h, the removal rate after five consecutive runs is only slightly changed and on the 5th regeneration cycle, the degradation efficiency of the MO under UV light is higher than 90% of the initial amount, as well as under the Visible light condition [52].
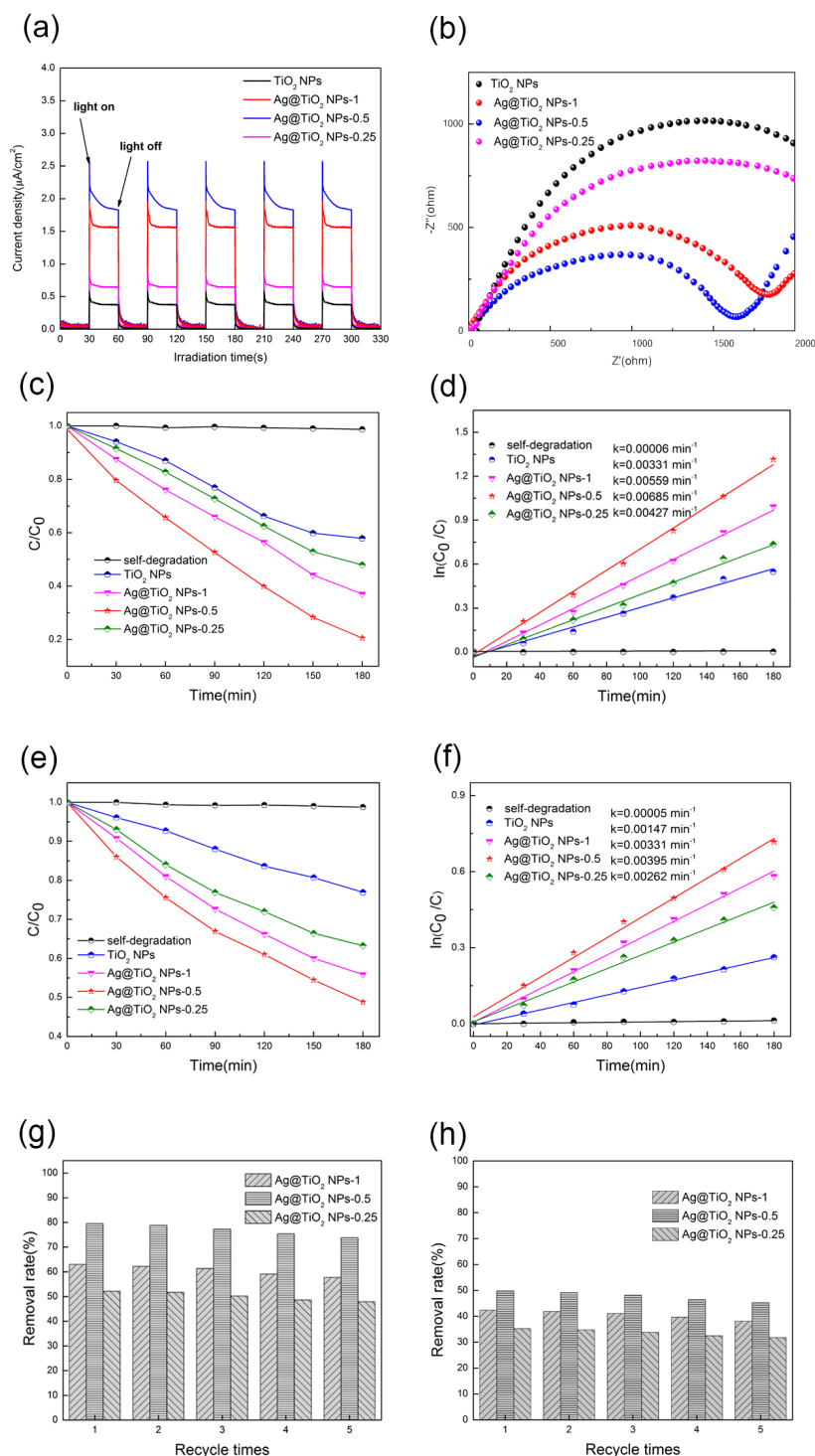
Figure 6. Photocurrent responses spectroscopy (**a**) and electrochemical impedance spectroscopy (EIS) (**b**) of the TiO_2 NPs and Ag@TiO_2 NPs samples; Methyl Orange (MO) photocatalytic degradation curves of the TiO_2 NPs and Ag@TiO_2 NPs samples under UV light (**c**); MO photocatalytic degradation Kinetic fit of the TiO_2 NPs and Ag@TiO_2 NPs samples under UV light (**d**); MO photocatalytic degradation curves of the TiO_2 NPs and Ag@TiO_2 NPs samples under Visible light (**e**); MO photocatalytic degradation Kinetic fit of the TiO_2 NPs and Ag@TiO_2 NPs samples under Visible light (**f**); Cycling performance of Ag@TiO_2 NPs samples for MO degradation under UV light (**g**); Cycling performance of Ag@TiO_2 NPs samples for MO degradation under Visible light (**h**).

It can be seen in Scheme 2 that a credible approach to enhance photocatalytic activity is proposed based on experimental analysis and discussion. On the one hand, Ag deposited NPs, a Schottky barrier has appeared at the interface between metal and semiconductor in UV light as a result of the lower Fermi level of Ag, and then the photoinduced electrons are transferred from the CB of TiO_2 to the Ag nanoparticles, promoting electron/hole pairs to separate [53,54]. What is more, the lifetimes of the charge carriers are increased, and the photocatalytic activity is improved because of the separation of photogenerated electrons and holes in this process. On the other hand, caused by the surface plasmon resonance effect, Ag nanoparticles are easily excited in the condition of being exposed to Visible light, which produces the large number of electrons on the surface. These electrons are transferred to the CB to enhance the absorbance value of TiO_2 in the Visible region [55,56]. During the photocatalytic process, the electrons accumulated on the TiO_2 react with the oxygen molecules existed on the surface or dissolved in the water, and are reduced to the activated superoxide anion radical$\cdot O_2^-$, which can remove organic pollutants or further generate oxides through a series of reactions with H^+. Meanwhile, holes can oxidize -OH or H_2O to strong oxidizing $\cdot OH$ radicals. Finally, strong oxidizing radicals $\cdot OH$ will oxidize MO to form CO_2 as well as a small number of partially oxidized intermediates [57,58].
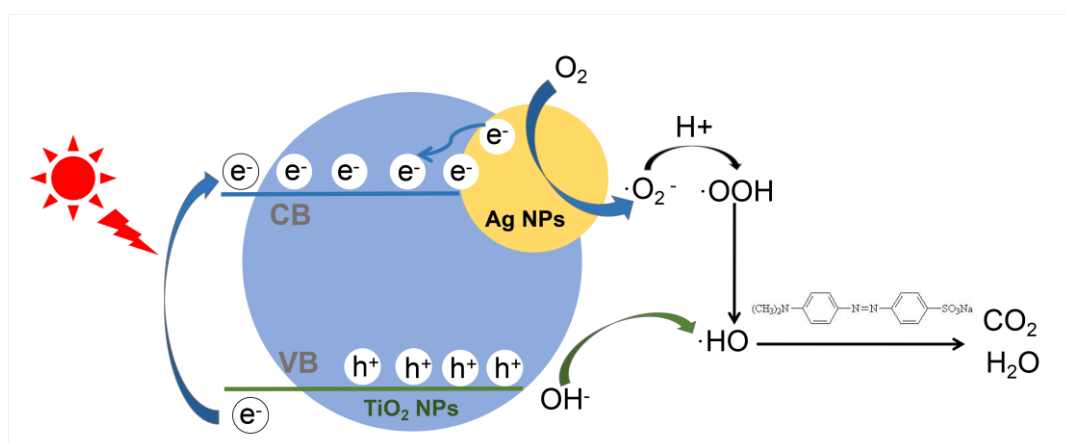
Scheme 2. Schematic diagram of electron transfer in Ag@TiO_2 NPs and degradation mechanism of MO.

4. Conclusions

In this work, a composite photocatalyst of TiO_2 NPs decorated with Ag NPs was prepared by the method of one-step synthesis, and the mass moral of PNP is also an important part in the dispersion and size of the growing particles in the hydrothermal reaction. The results indicate that Ag@TiO_2 NPs-0.5 shows the highest level of degradation efficiency, the mineralization rate of MO and shows the significant absorption range of Visible light. Beyond that, the Ag@TiO_2 NPs exhibit outstanding recyclability and retain over 90% of the original catalytic level for MO after five cycles of recycling. Therefore, there is a broad developing prospect in this work of photocatalytic hydrogen production, solar cells, sensors, rechargeable electrodes and exhaust gas treatment.

Author Contributions: Y.Z., D.Z. and Y.C. designed and conceived of the experiments; Y.Z. and F.F. performed the experiments; Y.L. and Y.Z. wrote the manuscript and analyzed the data.

Conflicts of Interest: The authors declare no conflicts of interest.

References

1. Wang, R.; Hashimot, K.; Fujishima, A.; Chikuni, M.; Kojima, E.; Kitamura, A.; Shimohigoshi, M.; Watanabe, T. Light-induced amphiphilic surfaces. *Nature* **1997**, *388*, 431–432. [CrossRef]
2. Xu, X.; Randorn, C.; Efstathiou, P.; Irvine, J.T. A red metallic oxide photocatalyst. *Nat. Mater.* **2012**, *11*, 595–598. [CrossRef] [PubMed]
3. Arul, N.S.; Mangalaraj, D.; Chen, P.C.; Ponpandian, N.; Meena, P.; Masuda, Y. Enhanced photocatalytic activity of cobalt-doped CeO_2, nanorods. *J. Sol-Gel Sci. Technol.* **2012**, *64*, 515–523. [CrossRef]
4. Kansal, S.K.; Kundu, P.; Sood, S.; Lamba, R.; Umar, A.; Mehta, S.K. Photocatalytic degradation of the antibiotic levofloxacin using highly crystalline TiO_2 nanoparticles. *New J. Chem.* **2014**, *38*, 3220–3226. [CrossRef]
5. Chan, S.C.; Barteau, M.A. Preparation of Highly Uniform Ag/TiO_2 and Au/TiO_2 Supported Nanoparticle Catalysts by Photodeposition. *Langmuir* **2005**, *21*, 5588–5595. [CrossRef] [PubMed]
6. Pumera, M.; Ambrosi, A.; Bonanni, A.; Chng, E.L.K.; Poh, H.L. Graphene for electrochemical sensing and biosensing. *Trac-Trends Anal. Chem.* **2010**, *29*, 954–965. [CrossRef]
7. Shen, X.; Zhu, L.; Liu, G.; Yu, H.; Tang, H. Enhanced Photocatalytic Degradation and Selective Removal of Nitrophenols by Using Surface Molecular Imprinted Titania. *Environ. Sci. Technol.* **2008**, *42*, 1687–1692. [CrossRef] [PubMed]
8. Shao, Y.; Wang, J.; Wu, H.; Liu, J.; Aksay, I.A.; Lin, Y. Graphene Based Electrochemical Sensors and Biosensors: A Review. *Electroanalysis* **2010**, *22*, 1027–1036. [CrossRef]
9. Wang, M.; Hu, Y.; Han, J.; Guo, R.; Xiong, H.; Yin, Y. TiO_2/NiO hybrid shells: P-n junction photocatalysts with enhanced activity under visible light. *J. Mater. Chem. A* **2015**, *3*, 20727–20735. [CrossRef]
10. An, H.; Park, S.Y.; Huh, J.Y.; Kim, H.; Lee, Y.C.; Lee, Y.B.; Hong, Y.C.; Lee, H.U. Nanoporous hydrogenated TiO_2 photocatalysts generated by underwater discharge plasma treatment for solar photocatalytic applications. *Appl. Catal. B* **2017**, *211*, 126–136. [CrossRef]
11. Shao, J.; Sheng, W.; Wang, M.; Li, S.; Chen, J.; Zhang, Y.; Cao, S. In situ synthesis of carbon-doped TiO_2 single-crystal nanorods with a remarkably photocatalytic efficiency. *Appl. Catal. B* **2017**, *209*, 311–319. [CrossRef]
12. Chai, X.; Zhang, H.; Cheng, C. 3D FTO inverse opals@hematite@TiO_2 hierarchically structured photoanode for photoelectrochemical water splitting. *Semicond Sci. Technol.* **2017**, *32*, 4003. [CrossRef]
13. Monfort, O.; Raptis, D.; Satrapinskyy, L.; Roch, T.; Plesch, G.; Lianos, P. Production of hydrogen by water splitting in a photoelectrochemical cell using a $BiVO_4/TiO_2$ layered photoanode. *Electrochim. Acta* **2017**, *251*, 244–249. [CrossRef]
14. Chen, Y.; Tang, Y.; Luo, S.; Liu, C.; Li, Y. TiO_2 nanotube arrays co-loaded with Au nanoparticles and reduced graphene oxide: Facile synthesis and promising photocatalytic application. *J. Alloys Compd.* **2013**, *578*, 242–248. [CrossRef]
15. Green, I.X.; Tang, W.; Neurock, M.; Yates, J.T. Localized partial oxidation of acetic acid at the dual perimeter sites of the Au/TiO_2 catalyst-formation of gold ketenylidene. *J. Am. Chem. Soc.* **2012**, *134*, 13569–13572. [CrossRef] [PubMed]
16. Pandikumar, A.; Sivaranjani, K.; Gopinath, C.S.; Ramaraj, R. Aminosilicate sol-gel stabilized N-doped TiO_2-Au nanocomposite materials and their potential environmental remediation applications. *RSC Adv.* **2013**, *3*, 13390–13398. [CrossRef]
17. Yu, Y.; Wen, W.; Qian, X.; Liu, J.; Wu, J. UV and visible light photocatalytic activity of Au/TiO_2 nanoforests with Anatase/Rutile phase junctions and controlled Au locations. *Sci. Rep.* **2017**, *7*, 41253. [CrossRef] [PubMed]
18. Xiang, X.; Yu, Y.; Wen, W.; Wu, J. Construction of hierarchical $Ag@TiO_2@ZnO$ nanowires with high photocatalytic activity. *New J. Chem.* **2017**, *42*, 265–271. [CrossRef]
19. Sun, T.; Liu, E.; Fan, J.; Hu, X.; Wu, F.; Hou, W.; Yang, Y.; Kang, L.; Hou, W.; Yang, Y.; et al. High photocatalytic activity of hydrogen production from water over Fe doped and Ag deposited anatase TiO_2 catalyst synthesized by solvothermal method. *Chem. Eng. J.* **2013**, *228*, 896–906. [CrossRef]

20. Yang, Y.; Liu, E.; Dai, H.; Kang, L.; Wu, H.; Fan, J.; Hu, X.; Liu, H. Photocatalytic activity of Ag-TiO$_2$-graphene ternary nanocomposites and application in hydrogen evolution by water splitting. *Int. J. Hydrogen Energy* **2014**, *39*, 7664–7671. [CrossRef]

21. Zhang, D.; Liu, X.; Li, J.; Xu, H.; Lin, H.; Chen, Y. Design and fabrication of a new class of nano hybrid materials based on reactive polymeric molecular cages. *Langmuir* **2013**, *29*, 11498–11505. [CrossRef] [PubMed]

22. Zhang, D.; Xiong, J.; Li, C.; Zhang, Y.; Toh, G.W.; Lin, H.; Chen, Y. Synthesis of size tunable gold nanoparticles polymeric hybrid based on molecular nanocages. *Micro Nano Lett.* **2014**, *9*, 235–238. [CrossRef]

23. Li, M.; Li, J.; Sun, H. Decolorizing of azo dye Reactive red 24 aqueous solution using exfoliated graphite and H$_2$O$_2$ under ultrasound irradiation. *Ultrason. Sonochem.* **2008**, *15*, 717–723. [CrossRef] [PubMed]

24. Jung, H.Y.; Yeo, I.S.; Kim, H.C.; Ki, H.C.; Gu, H.B. Surface plasmon resonance effect of silver nanoparticles on a TiO$_2$, electrode for dye-sensitized solar cells. *Appl. Surf. Sci.* **2017**, *432*, 266–271. [CrossRef]

25. Fu, F.; Wang, F.; Li, T.; Jiao, C.; Zhang, Y.; Chen, Y. Synthesis of TiO$_2$NWS@AuNPS Composite Catalyst for Methylene Blue Removal. *Materials* **2018**, *11*, 1022. [CrossRef] [PubMed]

26. Li, J.; Liu, X.; Wang, X.; Wang, R. Controlling nanoparticle formation via sizable cages of supramolecular soft materials. *Langmuir* **2011**, *27*, 7820–7827. [CrossRef] [PubMed]

27. Iwahori, K.; Takagi, R.; Kishimoto, N.; Yamashita, I. A size controlled synthesis of CuS nano-particles in the protein cage, apoferritin. *Mater. Lett.* **2011**, *65*, 3245–3247. [CrossRef]

28. Adachi, M.; Murata, Y.; Takao, J.; Jiu, J.; Sakamoto, M.; Wang, F. Highly Efficient Dye-Sensitized Solar Cells with a Titania Thin-Film Electrode Composed of a Network Structure of Single-Crystal-like TiO$_2$ Nanowires Made by the "Oriented Attachment" Mechanism. *J. Am. Chem. Soc.* **2004**, *126*, 14943–14949. [CrossRef]

29. Wang, P.; Han, L.; Zhu, C.; Zhai, Y.; Dong, S. Aqueous-phase synthesis of Ag-TiO$_2$-reduced graphene oxide and Pt-TiO$_2$-reduced graphene oxide hybrid nanostructures and their catalytic properties. *Nano Res.* **2011**, *4*, 1153–1162. [CrossRef]

30. An, T.; Yang, H.; Song, W.; Li, G.; Luo, H.; Cooper, W.J. Mechanistic Considerations for the Advanced Oxidation Treatment of Fluoroquinolone Pharmaceutical Compounds using TiO$_2$ Heterogeneous Catalysis. *J. Phys. Chem. A* **2010**, *114*, 2569–2575. [CrossRef]

31. Kulkarni, R.M.; Malladi, R.S.; Hanagadakar, M.S.; Doddamani, M.R.; Santhakumari, B.; Kulkarni, S.D. Ru-TiO$_2$, semiconducting nanoparticles for the photo-catalytic degradation of bromothymol blue. *J. Mater. Sci. Mater. Electron.* **2016**, *27*, 1–10. [CrossRef]

32. Leshuk, T.; Parviz, R.; Everett, P.; Krishnakumar, H.; Varin, R.A.; Gu, F. Photocatalytic activity of hydrogenated TiO$_2$. *ACS Appl. Mater. Interfaces* **2013**, *5*, 1892–1895. [CrossRef]

33. Yu, D.; Yu, X.; Wang, C.; Liu, X.; Xing, Y. Synthesis of Natural Cellulose-Templated TiO$_2$/Ag Nanosponge Composites and Photocatalytic Properties. *ACS Appl. Mater. Interfaces* **2012**, *4*, 2781–2787. [CrossRef] [PubMed]

34. Li, H.; Zeng, Y.; Huang, T.; Liu, M. Oxygen vacancies contained TiO$_2$ spheres: Facile fabrication and enhanced ferromagnetism. *J. Nanopart. Res.* **2012**, *14*, 1030. [CrossRef]

35. Xin, B.; Jing, L.; Ren, Z.; Wang, B.; Fu, H. Effects of simultaneously doped and deposited Ag on the photocatalytic activity and surface states of TiO$_2$. *J. Phys. Chem. B* **2005**, *109*, 2805–2809. [CrossRef] [PubMed]

36. Lin, D.; Wu, H.; Zhang, R.; Pan, W. Enhanced Photocatalysis of Electrospun Ag–ZnO Heterostructured Nanofibers. *Chem Mater.* **2009**, *21*, 3479–3484. [CrossRef]

37. Mino, L.; Spoto, G.; Bordiga, S.; Zecchina, A. Particles Morphology and Surface Properties As Investigated by HRTEM, FTIR, and Periodic DFT Calculations: From Pyrogenic TiO$_2$ (P25) to Nanoanatase. *J. Phys. Chem. C* **2012**, *116*, 17008–17018. [CrossRef]

38. Mino, L.; Spoto, G.; Bordiga, S.; Zecchina, A. Rutile Surface Properties beyond the Single Crystal Approach: New Insights from the Experimental Investigation of Different Polycrystalline Samples and Periodic DFT Calculations. *J. Phys. Chem. C* **2013**, *117*, 11186–11196. [CrossRef]

39. Mino, L.; Zecchina, A.; Martra, G.; Rossi, A.M.; Spoto, G. A surface science approach to TiO$_2$ P25 photocatalysis: An in situ FTIR study of phenol photodegradation at controlled water coverages from sub-monolayer to multilayer. *Appl. Catal. B-Environ.* **2016**, *196*, 135–141. [CrossRef]

40. Li, F.B.; Li, X.Z. The enhancement of photodegradation efficiency using Pt–TiO$_2$ catalyst. *Chemosphere* **2002**, *21*, 1103–1111. [CrossRef]

41. Colthup, N.B. Spectra-Structure Correlations in the Infra-Red Region. *J. Opt. Soc. Am.* **1950**, *4*, 421. [CrossRef]

42. Reddy, D.A.; Lee, S.; Choi, J.; Park, S.; Ma, R.; Yang, H.; Kim, T.K. Green synthesis of AgI-reduced graphene oxide nanocomposites: Toward enhanced visible-light photocatalytic activity for organic dye removal. *Appl. Surf. Sci.* **2015**, *341*, 175–184. [CrossRef]

43. Reddy, D.A.; Choi, J.; Lee, S.; Ma, R.; Kim, T.K. Green synthesis of AgI nanoparticle-functionalized reduced graphene oxide aerogels with enhanced catalytic performance and facile recycling. *RSC Adv.* **2015**, *5*, 67394–67404. [CrossRef]

44. Choi, J.; Reddy, D.A.; Kim, T.K. Enhanced photocatalytic activity and anti-photocorrosion of AgI nanostructures by coupling with graphene-analogue boron nitride nanosheets. *Ceram. Int.* **2015**, *41*, 13793–13803. [CrossRef]

45. Islam, M.J.; Reddy, D.A.; Ma, R.; Kim, Y.; Kim, T.K. Reduced-graphene-oxide-wrapped BiOI-AgI heterostructured nanocomposite as a high-performance photocatalyst for dye degradation under solar light irradiation. *Solid State Sci.* **2016**, *61*, 32–39. [CrossRef]

46. Ma, R.; Islam, M.J.; Reddy, D.A.; Kim, T.K. Transformation of CeO_2 into a mixed phase CeO_2/Ce_2O_3 nanohybrid by liquid phase pulsed laser ablation for enhanced photocatalytic activity through Z-scheme pattern. *Ceram. Int.* **2016**, *42*, 18495–18502. [CrossRef]

47. Lee, S.; Reddy, D.A.; Kim, T.K. Well-wrapped reduced graphene oxide nanosheets on $Nb_3O_7(OH)$ nanostructures as good electron collectors and transporters for efficient photocatalytic degradation of rhodamine B and phenol. *RSC Adv.* **2016**, *6*, 37180–37188. [CrossRef]

48. Reddy, D.A.; Reddy, D.A.; Ma, R.; Choi, M.Y.; Kim, T.K. Reduced graphene oxide wrapped ZnS–Ag2S ternary composites synthesized via hydrothermal method: Applications in photocatalyst degradation of organic pollutants. *Appl. Surf. Sci.* **2015**, *324*, 725–735. [CrossRef]

49. Sun, C.; Xu, Q.; Xie, Y.; Ling, Y.; Hou, Y. Designed synthesis of anatase-TiO_2 (B) biphase nanowires/ZnO nanoparticles heterojunction for enhanced photocatalysis. *J. Mater. Chem. A* **2018**, *6*, 8289–8298. [CrossRef]

50. Islam, M.J.; Kim, H.K.; Reddy, D.A.; Kim, Y.; Ma, R.; Baek, H.; Kim, J.; Kim, T.K. Hierarchical BiOI nanostructures supported on a metal organic framework as efficient photocatalysts for degradation of organic pollutants in water. *Dalton Trans.* **2017**, *46*, 6013–6023. [CrossRef]

51. Reddy, D.A.; Choi, J.; Lee, S.; Kim, T.K. Controlled synthesis of heterostructured Ag@AgI/ZnS microspheres with enhanced photocatalytic activity and selective separation of methylene blue from mixture dyes. *J. Taiwan Inst. Chem. Eng.* **2016**, *66*, 200–209. [CrossRef]

52. Islam, M.J.; Reddy, D.A.; Han, N.S.; Choi, J.; Song, J.K.; Kim, T.K. An oxygen-vacancy rich 3D novel hierarchical MoS2/BiOI/AgI ternary nanocomposite: Enhanced photocatalytic activity through photogenerated electron shuttling in a Z-scheme manner. *Phys. Chem. Chem. Phys.* **2016**, *18*, 24984–24993. [CrossRef]

53. Arshadi, M.; Mousavinia, F.; Amiri, M.J.; Faraji, A.R. Adsorption of methyl orange and salicylic acid on a nano-transition metal composite: Kinetics, thermodynamic and electrochemical studies. *J. Colloid Interface Sci.* **2016**, *483*, 118–131. [CrossRef] [PubMed]

54. Islam, M.J.; Reddy, D.A.; Choi, J.; Kim, T.K. Surface oxygen vacancy assisted electron transfer and shuttling for enhanced photocatalytic activity of a Z-scheme CeO_2–AgI nanocomposite. *RSC Adv.* **2016**, *6*, 19341–19350. [CrossRef]

55. Liu, X.; Xing, Z.; Zhang, Y.; Li, Z.; Wu, X.; Tan, S.; Yu, X.; Zhu, Q.; Zhou, W. Fabrication of 3D flower-like black N-TiO_2x@MoS2 for unprecedented-high visible-light-driven photocatalytic performance. *Appl. Catal. B-Environ.* **2017**, *201*, 119–127. [CrossRef]

56. Ma, J.; Guo, S.; Guo, X.; Ge, H. A mild synthetic route to Fe_3O_4@TiO_2-Au composites: Preparation, characterization and photocatalytic activity. *Appl. Surf. Sci.* **2015**, *353*, 1117–1125. [CrossRef]

57. Choi, J.; Reddy, D.A.; Islam, M.J.; Ma, R.; Kim, T.K. Self-assembly of CeO_2 nanostructures/reduced graphene oxide composite aerogels for efficient photocatalytic degradation of organic pollutants in water. *J. Alloys Compd.* **2016**, *688*, 527–536. [CrossRef]

58. Yang, B.; He, D.; Wang, W.; Zhuo, Z.; Wang, Y. Gold-plasmon enhanced photocatalytic performance of anatase titania nanotubes under visible-light irradiation. *Mater. Res. Bull.* **2016**, *74*, 278–283. [CrossRef]